Volume 9 | Number 12 | 28 March 2017 | Pages 4037–4312

Nanoscale

rsc.li/nanoscale

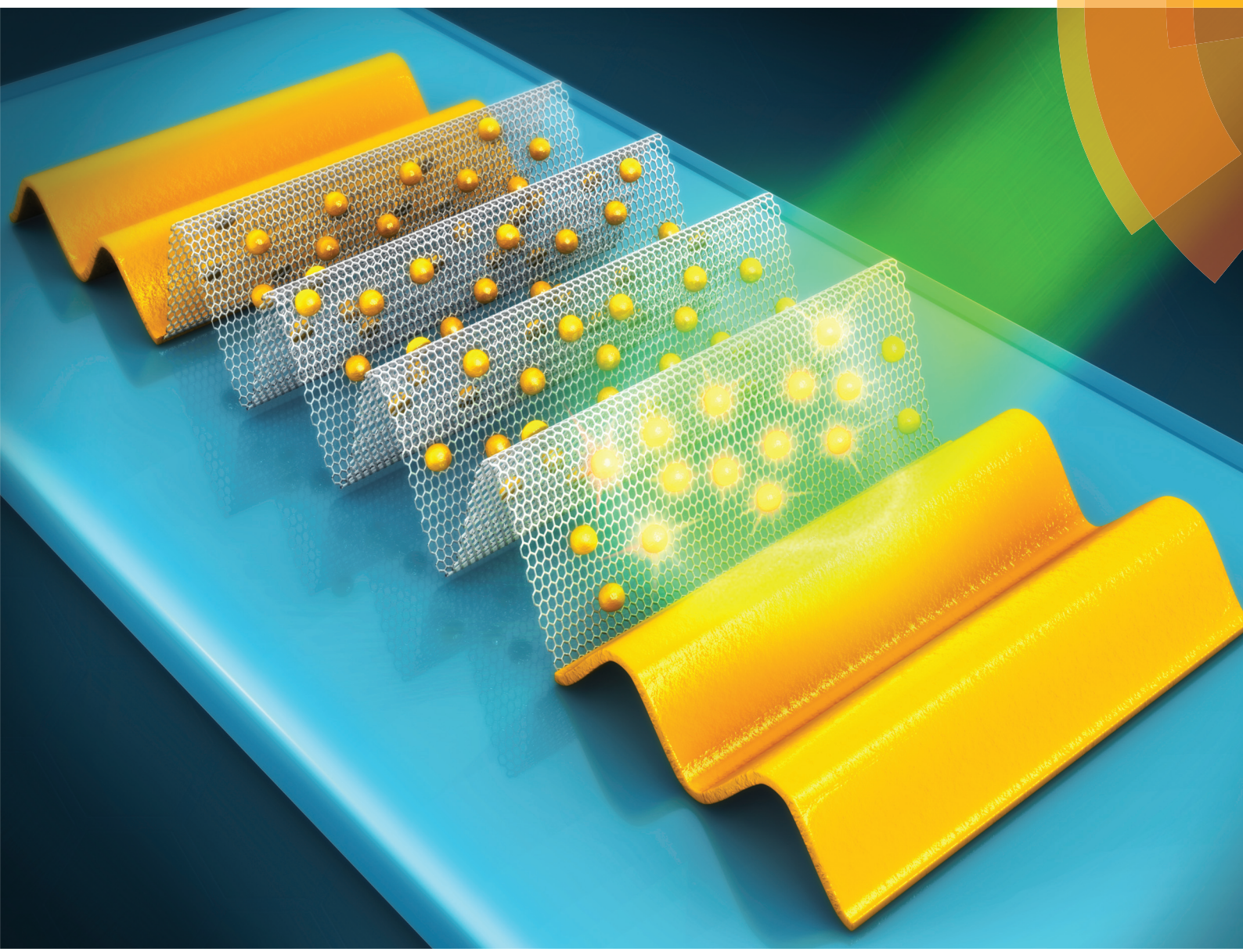

ISSN 2040-3372

ROYAL SOCIETY OF CHEMISTRY

PAPER
SungWoo Nam *et al.*
A stretchable crumpled graphene photodetector with plasmonically enhanced photoresponsivity

NCNST

Nanoscale

PAPER

View Article Online
View Journal | View Issue

Cite this: *Nanoscale*, 2017, **9**, 4058

A stretchable crumpled graphene photodetector with plasmonically enhanced photoresponsivity†

Minsu Kim,‡[a] Pilgyu Kang,‡[b] Juyoung Leem‡[b] and SungWoo Nam*[a,b]

Received 1st December 2016,
Accepted 12th January 2017

DOI: 10.1039/c6nr09338h

rsc.li/nanoscale

Graphene has been widely explored for flexible, high-performance photodetectors due to its exceptional mechanical strength, broadband absorption, and high carrier mobility. However, the low stretchability and limited photoabsorption of graphene have restricted its applications in flexible and highly sensitive photodetection systems. Various hybrid systems based on photonic or plasmonic nanostructures have been introduced to improve the limited photoresponsivity of graphene photodetectors. In most cases, the hybrid systems succeeded in the enhancement of photoresponsivity, but showed limited mechanical stretchability. Here, we demonstrate a stretchable photodetector based on a crumpled graphene–gold nanoparticle (AuNP) hybrid structure with ~1200% enhanced photoresponsivity, compared to a conventional flat graphene-only photodetector, and exceptional mechanical stretchability up to a 200% tensile strain. We achieve plasmonically enhanced photoresponsivity by integrating AuNPs with graphene. By crumpling the hybrid structure, we realize mechanical stretchability and further enhancement of the optical absorption by densification. We also demonstrate that our highly stretchable photodetector with enhanced photoresponsivity can be integrated on a contact lens and a spring structure. We believe that our stretchable, high performance graphene photodetector can find broad applications for conformable and flexible optical sensors and dynamic mechanical strain sensors.

Introduction

Recently, flexible optoelectronic devices have been actively developed for diverse applications, including sensing in biological systems,[1–3] wearable optoelectronic devices,[4] and flexible integrated photonics.[5,6] As one of the key components in optoelectronic devices, a highly flexible photodetector with high photoresponsivity has been specifically desired for advanced applications such as human health monitoring devices[2,3,7] and wearable electronics.[1,2,4] Graphene, a single layer of hexagonally bonded carbon atoms,[8] has been considered an attractive optical/optoelectronic material for flexible photodetectors because of its outstanding mechanical strength,[9,10] broadband absorption from ultraviolet to terahertz frequencies,[11–13] and high carrier mobility.[14,15] Despite its exceptional mechanical, optical, and electrical properties, graphene-based photodetectors have been hardly applied to flexible and stretchable optoelectronic devices for two primary reasons: graphene shows only limited stretchability – specifically, ~6% for the chemical vapour deposition (CVD) synthesized polycrystalline graphene[16] and 25% for the mechanically exfoliated graphene[9] without structural failure; additionally, the low light absorption of a single layer graphene (~2.3%),[17,18] attributed to its atomically thin structure, presents another challenge in developing flexible graphene-based photodetectors.

The limited mechanical stretchability of graphene can be improved by creating an elastically buckle-delaminated structure of graphene (*i.e.*, graphene crumples[19–21]). The crumpled graphene was fabricated by delamination-buckling of graphene on a polymer substrate as applied tensile strain is released from the polymer substrate.[21,22] The crumpled graphene allowed high stretchability and increased optical absorption, led by the enhanced areal density of graphene. Although the crumpled graphene has shown high stretchability, up to 200% tensile strain, the photoresponsivity of the crumpled graphene photodetector remained limited.

Various approaches to integrating graphene with photonic nanostructures[13,23–31] or with other photonic materials (*e.g.*, quantum dots,[32–34] nanowires[35–37] and transition metal dichalcogenide monolayers[38]) have been explored for enhanced photoresponsivity. Even though the integration enabled high photoresponsivity, most graphene-based photodetectors with the hybrid approaches still have limited stretchability.[13,23–27,31]

[a]*Department of Materials Science and Engineering, University of Illinois at Urbana-Champaign, Urbana, Illinois 61801, USA. E-mail: swnam@illinois.edu*
[b]*Department of Mechanical Science and Engineering, University of Illinois at Urbana-Champaign, Urbana, Illinois 61801, USA*

†Electronic supplementary information (ESI) available. See DOI: 10.1039/c6nr09338h

‡These authors contributed equally to this work.

Recently, Chiang *et al.*[32] reported a stretchable photodetector based on the hybrid structure of graphene and graphene quantum dots with high photoresponsivity. However, their photodetector has a limited stretchability – only up to 25%. Furthermore, mechanical robustness was demonstrated only up to 30 cycles of mechanical stretching.

Integrating plasmonic nanostructures with graphene demonstrated the possibility of effectively enhancing optical absorption by a strong field enhancement.[29–31] Liu *et al.*[31] reported a photodetector with the AuNP array on graphene which exhibited 1500% higher photoresponsivity compared to that without the AuNP array. The photoresponsivity was plasmonically enhanced by the excited surface plasmons confined in the plasmonic nanostructure. In addition, in our recent studies,[39] we demonstrated the plasmonically enhanced surface enhanced Raman spectroscopy by crumpling the graphene–AuNP hybrid structure using a heat shrinkable polymer.

Here, we present a photodetector based on crumpled graphene integrated with AuNPs, which shows enhanced mechanical stretchability and photoresponsivity (Fig. 1a). To achieve high stretchability, the crumpled graphene–AuNP hybrid structure was formed by buckle-delamination of the hybrid film using an elastomeric substrate. Crumpling also enables the enhanced photoresponsivity, which is led by optical absorption enhancement, by the areal densification of graphene[21] and consequently, the number density increase of AuNPs. AuNPs themselves are plasmonic nanostructures, and the increased number of AuNPs per projected unit area further enhances the plasmonic enhancement of optical absorption.[39–41] As a result, our photodetector shows not only over an order-of-magnitude higher enhancement (~1200%) of photoresponse compared to a flat graphene photodetector, but also outstanding mechanical stretchability up to 200%, together with the strain-tunable photoresponsivity. Finally, we demonstrate the potential of our stretchable photodetector with plasmonically enhanced photoresponsivity for various applications – for example, biomedical optical sensors[41,42] and dynamic mechanical strain sensors.[43]

Results and discussion

To achieve crumpled hybrid structures, we first fabricate graphene–AuNP hybrid structures by using the approach previously demonstrated.[39] Briefly, we deposited a 3 nm thick gold thin film on the CVD-grown graphene, and thermally annealed the graphene–Au composite film to fabricate the graphene–AuNP hybrid film (see the ESI† for more details). Then, the hybrid film was transferred on a biaxially pre-strained very high bond (VHB) film ($\varepsilon_{x,\mathrm{pre},1}$ = 350% and $\varepsilon_{y,\mathrm{pre},1}$ = 250%) (Fig. 1b). The VHB substrate allowed our highly stretchable photodetector with stretchability up to a 200% tensile strain compared to a polydimethylsiloxane (PDMS) substrate with

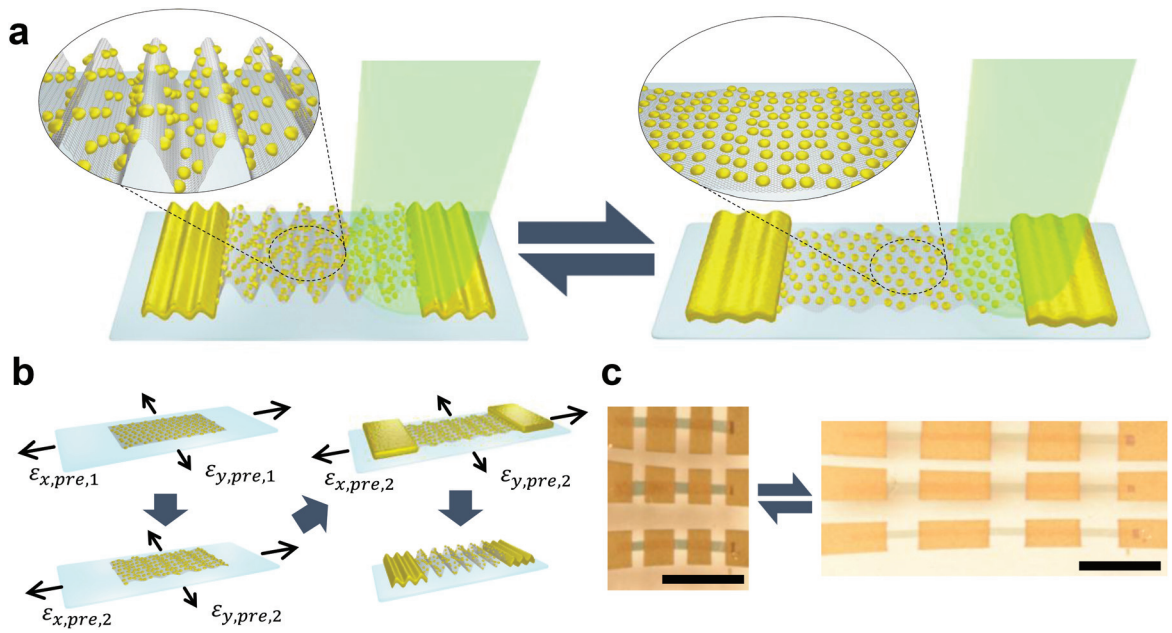

Fig. 1 Schematic illustrations of a stretchable photodetector with crumpled graphene–gold nanoparticle (AuNP) hybrid structure and its fabrication procedures, and photographs of the fabricated photodetector device array. (a) Schematic illustration of the stretchable photodetector with the crumpled graphene–AuNP hybrid structures (left). As uniaxial tensile strain is applied, the crumpled hybrid structure is uncrumpled (right). (b) Fabrication procedure of the crumpled hybrid photodetector. The graphene–AuNP hybrid film is transferred onto a biaxially pre-strained highly stretchable polymer substrate ($\varepsilon_{x,\mathrm{pre},1}$ and $\varepsilon_{y,\mathrm{pre},1}$), followed by a sequential release that leads to the crumpled hybrid structure. Gold metal contacts are thermally deposited on the biaxially pre-stretched crumpled hybrid film on the stretchable substrate ($\varepsilon_{x,\mathrm{pre},2}$ and $\varepsilon_{y,\mathrm{pre},2}$). Sequential release of the pre-stretching results in the stretchable hybrid photodetector. (c) Photographs of the fabricated stretchable hybrid photodetector array (an array of 3 × 3 photodetector devices, scale bars = 3 mm). The crumpled hybrid photodetectors were fabricated with pre-strains of $\varepsilon_{x,\mathrm{pre},1}$ = 350% and $\varepsilon_{y,\mathrm{pre},1}$ = 250%. The photographs on the left and the right sides show the array device at $\varepsilon_{\mathrm{tensile},x}$ = 0% and 200% respectively.

stretchability up to 40%.[44] A sequential release of the pre-strained VHB film yielded deterministically formed crumpled structures through buckle-delamination of the hybrid film. Then, gold contacts were deposited at both ends of a re-stretched ($\varepsilon_{x,\mathrm{pre},2}$ and $\varepsilon_{y,\mathrm{pre},2}$) crumpled hybrid structure for photoresponse characterization. The fabrication of a photodetector device was completed by releasing the whole structure. Fig. 1c shows a photo of a fabricated photodetector array device.

We performed detailed material characterization of crumpled hybrid structures with scanning electron microscopy (SEM), Raman spectroscopy, and ultraviolet-visible (UV-Vis) spectroscopy. First, we conducted SEM imaging to investigate the morphology of AuNPs on graphene and the topography of the crumpled hybrid structures (Fig. 2a–c). In the SEM image prior to crumpling (Fig. 2a), AuNPs were observed to be highly dense and monodispersed. The average diameter and gap-distance between adjacent AuNPs were estimated to be 67.0 ± 2.82 nm and 36.5 nm respectively (see the ESI† for more details). Fig. 2b shows the SEM image of the crumpled hybrid structure fabricated with prestrains of $\varepsilon_{x,\mathrm{pre},1}$ = 350% and $\varepsilon_{y,\mathrm{pre},1}$ = 250%. The crumpled hybrid structures were highly ordered, and the crumple wavelength in the x-direction was determined to be ~280 nm through SEM image analysis, which is close to ~300 nm predicted by an analytical model[9,22,45] (see the ESI† for more details). Fig. 2c shows the SEM image of the crumpled hybrid structure obtained with uniaxial stretching in the x-direction by a 200% stretching strain after one hundred cycles of re-stretching ($\varepsilon_{\mathrm{tensile},x}$ = 200%) and relaxation. The dominantly induced crumples were uncrumpled, whereas crumples in the other direction were formed due to Poisson's effect. We also confirmed robust structural integrity between graphene and AuNPs with respect to the cyclic stretching strains.

We further carried out Raman spectroscopy of the crumpled hybrid structures at varying uniaxial tensile strains between 0% and 200% (Fig. 2d). Crumpled graphene exhibited three characteristic bands at 1350 cm^{-1}, 1580 cm^{-1}, and 2690 cm^{-1} (D, G, and 2D, respectively). The relatively small intensity of the D peak indicated that no significant defects were present in the crumpled hybrid structure. Furthermore, the crumpled graphene–AuNP hybrid structures showed consistently small D

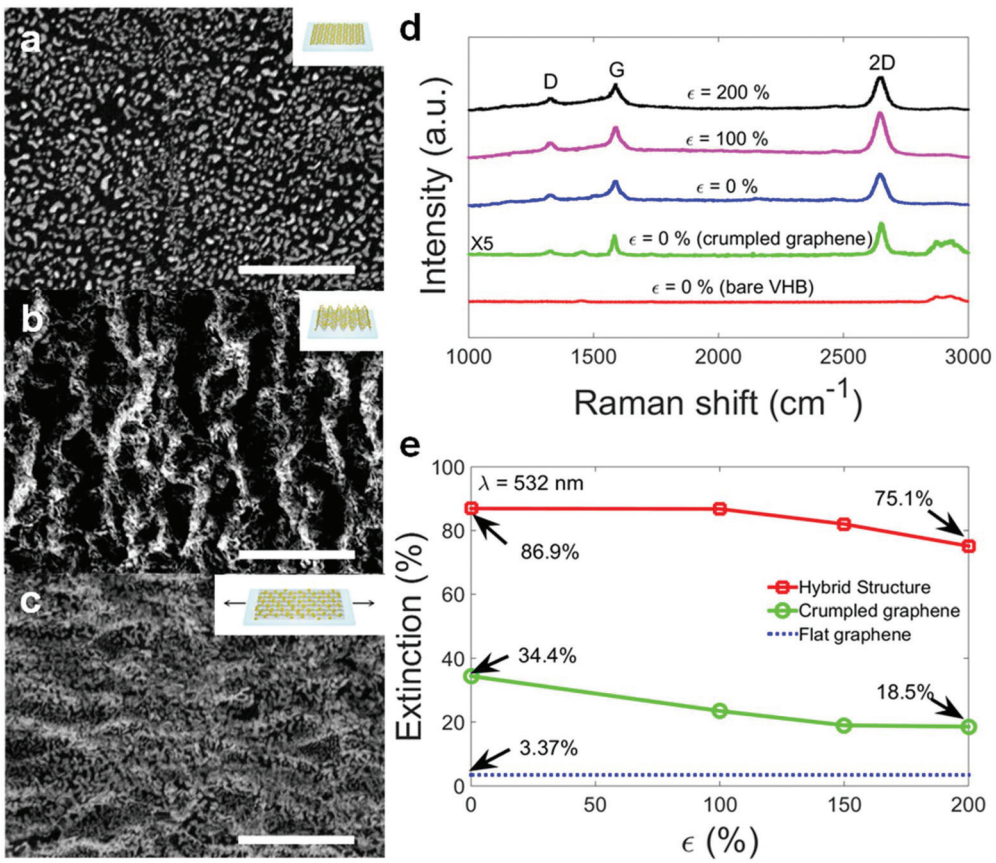

Fig. 2 Material characterization of crumpled graphene–AuNP hybrid structures. SEM images of a flat hybrid structure (a) and the crumpled hybrid structure at re-stretching strains, $\varepsilon_{\mathrm{tensile},x}$ = 0% (b) and 200% (c). The crumpled hybrid structures were fabricated with pre-strains of $\varepsilon_{x,\mathrm{pre},1}$ = 350%, $\varepsilon_{y,\mathrm{pre},1}$ = 250%. (d) Raman spectra of the crumpled hybrid structure on a VHB substrate at varying uniaxial tensile strains ($\varepsilon_{\mathrm{tensile},x}$ = 0%, 100%, 200%), a flat graphene on a VHB substrate, and a bare VHB film. (e) Optical extinction at λ_{light} = 532 nm of the crumpled hybrid structure on a VHB substrate, and the crumpled graphene on a VHB substrate at varying uniaxial tensile strains ($\varepsilon_{\mathrm{tensile},x}$ = 0%, 100%, 200%), and flat graphene on VHB substrate. All scale bars are 1 μm.

peak intensities at varying tensile strains between 0% and 200%, similar to that of the crumpled graphene. These results imply negligible defects in the crumpled hybrid structures and mechanical robustness of the structure in re-stretching strains up to $\varepsilon_{\text{tensile},x}$ = 200%.

We performed UV-Vis spectroscopy to investigate the strain tunability and enhancement of photoabsorption (Fig. 2e and S1 in the ESI†). We also quantitatively characterized the mechanical integrity of the crumpled hybrid structure by UV-Vis spectroscopy with respect to one thousand cycles of varying tensile strains between 0% and 200% (Fig. S2 in the ESI†). The wavelength λ_{light} = 532 nm was selected in Fig. 2e because it is widely used in biosensing applications.[46] In addition, we observed a relatively large optical extinction difference between $\varepsilon_{\text{tensile},x}$ = 0% and 200% at the wavelength where a large tunability of photoresponse was achievable (Fig. S1 in the ESI†).

To investigate strain-tunable photoabsorption, we compared the optical extinction of crumpled hybrid structures at $\varepsilon_{\text{tensile},x}$ = 0% and 200%. Re-stretching from $\varepsilon_{\text{tensile},x}$ = 0% to $\varepsilon_{\text{tensile},x}$ = 200% results in the areal density decrease of graphene, and simultaneously, the number density decrease of AuNPs. The relationship between re-stretching and photoabsorption change can be explained analytically. The number density ($\rho_{N,0}$) of AuNPs in a flat graphene–AuNP hybrid structure was estimated to be 123 ± 13 particles per μm^2 (see Fig. S3 and S4 in the ESI†). The number density of AuNPs in the crumpled graphene–AuNP hybrid structure was estimated with the theoretical ratio (d_c)[47] of the crumpled surface area to its projected flat area and with consideration of Poisson's effect. With calculated d_c values and experimentally measured Poisson's ratio, ν_{VHB} = 0.2, the number density of AuNPs is estimated to be ≈640 particles per μm^2 at $\varepsilon_{\text{tensile},x}$ = 0% and ≈505 particles per μm^2 at $\varepsilon_{\text{tensile},x}$ = 200% (see the ESI† for more details). The calculated AuNP number density at $\varepsilon_{\text{tensile},x}$ = 200% is reduced by 21.5% from that at $\varepsilon_{\text{tensile},x}$ = 0%. The calculated number density reduction is close to measured optical extinction reduction of ~14% (86.9% → 75.1%). Furthermore, the crumpled hybrid structure showed consistent optical extinction at varying tensile strains in the UV-Vis measurements in one thousand cycles of uniaxial stretching–relaxation (Fig. S2 in the ESI†), and such results demonstrated robust tunability.

To further investigate the photoabsorption enhancement of the hybrid structure, we compared the optical extinction of crumpled hybrid structures with that of crumpled graphene and flat graphene. First, the optical extinction of the crumpled graphene at $\varepsilon_{\text{tensile},x}$ = 0% was 10.2 times larger than that of flat graphene. The areal density increase of crumpled graphene yields higher light absorption. Second, the optical extinction of crumpled hybrid structures at $\varepsilon_{\text{tensile},x}$ = 0% was 2.52 times larger than that of the crumpled graphene at $\varepsilon_{\text{tensile},x}$ = 0%. The photoabsorption enhancement of the crumpled hybrid structure is attributable to the two mechanisms of plasmonic enhancement by AuNPs:[31] (1) localized surface plasmons of AuNPs enhance local electromagnetic fields in AuNPs, and (2) the plasmonic energy absorbed in one nanoparticle decays radiatively and interacts with other neighbouring nanoparticles.[48]

To show plasmonically enhanced, strain-tunable photoresponse together with mechanical stretchability, we fabricated and characterized a photodetector based on the crumpled hybrid structure. We performed dynamic photocurrent measurements to characterize the photoresponse of the crumpled hybrid photodetector to 532 nm laser light. A 532 nm wavelength laser beam was focused at the junction of the photoconductive channel made of the crumpled hybrid structure and the gold electrode to measure the maximum photocurrent.[21,31] The laser was turned on and off every 15 seconds for three cycles. For comparison, a crumpled graphene photodetector and a flat graphene photodetector were fabricated with similar device dimensions, including channel length and width. The dynamic photoresponses of the crumpled graphene photodetector and the flat graphene photodetector were characterized similarly as the crumpled hybrid photodetector. The measured photocurrents were normalized with the maximum photocurrent value of the crumpled hybrid photodetector at $\varepsilon_{\text{tensile},x}$ = 0% (Fig. 3a).

With consideration of the characterization of optical extinction, we compared the photoresponse of our hybrid photodetector with a flat graphene photodetector and a crumpled graphene photodetector. The measured photocurrent of the crumpled hybrid photodetector was 1570% and 110% larger than that of the flat graphene photodetector and the crumpled graphene photodetector, respectively (Fig. 3b). The photoresponsivity ($R_{\text{ph}} = I_{\text{ph}}/P_{\text{in}}$) of the crumpled hybrid photodetector was estimated to be 0.044 mA W^{-1} (see Table S1 in the ESI†), which was ~2.3 times larger than that of a crumpled graphene photodetector and ~12 times larger than the flat graphene photodetector's photoresponsivity. The optical extinction enhancement factor due to crumpling, $\sigma_{\text{ext,crumpled}}/\sigma_{\text{ext,flat}}$ = 34.4%/3.37% ≈ 10.2 (Fig. 2e), attributable to the areal density increase, was close to the photoresponse enhancement, $I_{\text{ph,crumpled}}/I_{\text{ph,flat}}$ = 0.47/0.06 ≈ 7.83 (Fig. 3b and Table S2 in the ESI†). Furthermore, the optical extinction enhancement factor due to AuNPs, $\sigma_{\text{ext,hybrid}}/\sigma_{\text{ext,crumpled}}$ = 86.9%/34.4% ≈ 2.53 (Fig. 2e), attributable to plasmonic enhancement, was also well-matched with the photoresponse enhancement, $I_{\text{ph,hybrid}}/I_{\text{ph,crumpled}}$ = 1/0.47 ≈ 2.13 (Fig. 3b and Table S2 in the ESI†). This consistency in values indicates that enhanced photoabsorption led to the enhancement of photoresponsivity. The small difference between the enhancement factor and photoresponsivity ratio is attributable to the scattering of photoexcited carriers in the crumpled plasmonic hybrid structures.

Furthermore, we examined the tunability of the photoresponse of the crumpled hybrid photodetector by applying tensile strains. The measured photocurrent at $\varepsilon_{\text{tensile},x}$ = 0% showed ~20% larger photocurrent compared to that at $\varepsilon_{\text{tensile},x}$ = 200% (Fig. 3b). The tunable extent of photoresponse was closely matched to that of optical extinction (15%). The strain-tunable photoresponse was consistent in multiple cycles of stretching and release (Fig. 3c). In addition, the mechanical robustness of

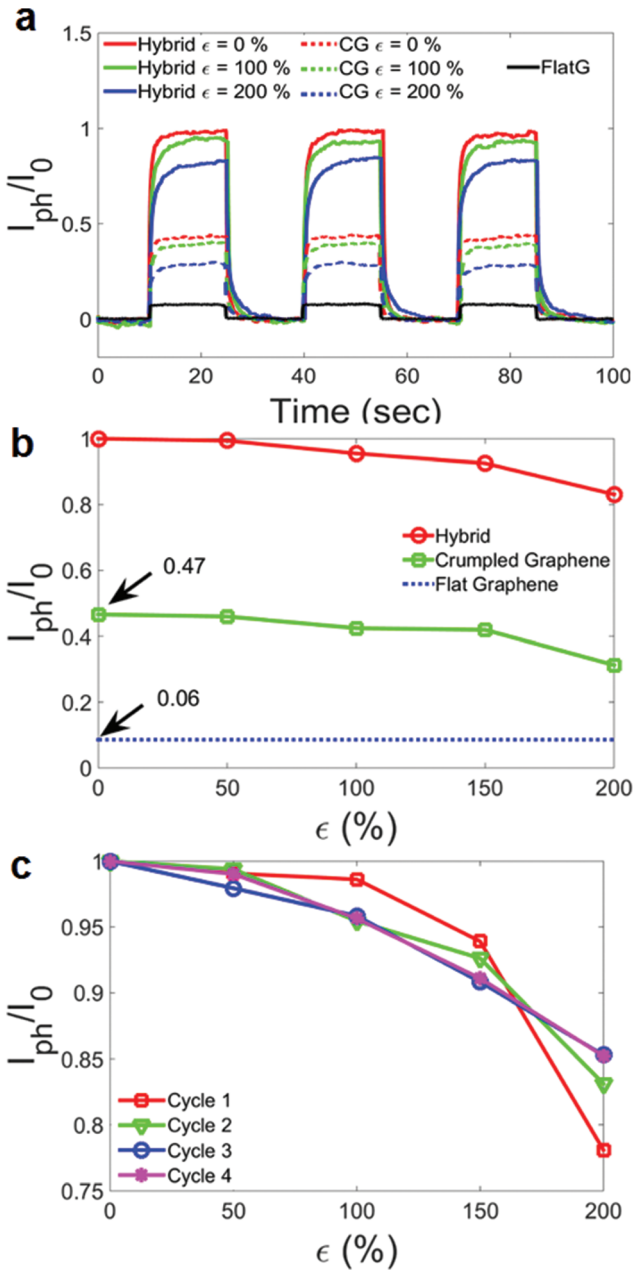

Fig. 3 Photoresponse characterization of a stretchable hybrid photodetector with crumpled graphene–AuNP hybrid structure. (a) Dynamic photoresponse at λ_{light} = 532 nm of the crumpled hybrid photodetector and a crumpled graphene photodetector at varying uniaxial tensile strains between 0% and 200%, and that of a flat graphene photodetector. All measured photocurrents were normalized with the photocurrent of the crumpled hybrid photodetector measured at $\varepsilon_{tensile,x}$ = 0%, denoted by I_0. (b) Comparison of the normalized photocurrents, I_{ph}/I_0, of the crumpled hybrid photodetector, and the crumpled graphene photodetector at the varying uniaxial tensile strains, and that of the flat graphene device. (c) Photocurrent measurements of the crumpled hybrid photodetector with multiple cycles of uniaxial tensile strains between 0% and 200%.

the crumpled hybrid photodetector was tested with respect to one thousand cycles of cyclic stretching (Fig. S5 in the ESI†). Photocurrents measured at $\varepsilon_{tensile,x}$ = 100% were consistent throughout one thousand cycles of cyclic stretching. Such results demonstrated the mechanical robustness of the strain-tunable photoresponse of our hybrid photodetector.

Moreover, we measured the resistance change of our crumpled hybrid photodetector with multiple cycles of tensile strains between 0% and 200%. The resistance (R) of our crumpled hybrid photodetector without light illumination was larger by a factor of 20–30, compared to the photoresistance ($R_p = V_{bias}/I_{ph}$), the resistance of our crumpled hybrid photodetector with light illumination. The increase in R showed a dissimilar trend from $\varepsilon_{tensile}$ = 0% to $\varepsilon_{tensile}$ = 200% ($\Delta R/R_0/\varepsilon \approx 0.2$), compared to the change in R_p ($\Delta R_p/R_{p,0}/\varepsilon \approx 0.09$) (Fig. S6a in the ESI†). The disparate trend indicates that tunable photoabsorption enabled by uncrumpling of the crumpled hybrid structures and the photoinduced effect in our crumpled hybrid structures have dominant effects on the modulated photoresponse over stretching. Moreover, the change in the measured photocurrent, $I_{ph} - I_{bias}$, normalized by the photocurrent measured at $\varepsilon_{x,tensile}$ = 0% (I_0) with respect to ε (Fig. S6b in the ESI†) showed a similar trend to that in Fig. 3c.

Finally, we demonstrated the potential use of our stretchable photodetector as a flexible and conformal optical sensor. We showed that our hybrid photodetector can be conformably integrated on the curved surface of a contact lens which applied bending strains to our hybrid photodetector device (Fig. 4a). The dynamic photocurrent was measured with respect to three on–off cycles of 532 nm laser light. The measured photocurrent exhibited a high signal-to-noise ratio through the cyclic switching of light (Fig. 4b and ESI Movie S1†). Such results demonstrated strain-tolerant photosensing, especially with respect to bending strains. This demonstration shows that our hybrid photodetector with enhanced photoresponsivity and high flexibility has the potential for wearable optical sensors and broad applications of human health monitoring.

Moreover, we showed a dynamic mechanical strain sensing by using the stain-tunable photoresponse and high stretchability. Our hybrid photodetector was integrated onto a spring (Fig. 4c). Photocurrents were measured with respect to cyclic on–off of 532 nm laser light at varying tensile strains between 0% and 200% applied to the spring (Fig. 4d). While stretching the spring, the measured photocurrent was decreased as the photoresponse of the crumpled hybrid photodetector was reduced at increased tensile strains. The reduction of the measured photocurrent was consistent with our earlier photoresponse characterization results (Fig. 3c). Our hybrid photodetector has the potential to be applicable to the suspension spring for an automotive vehicle when it is integrated with a light emitting diode, and the integrated system can monitor the strain variance from shock loads more efficiently. In addition, a photodetector with a large strain sensing capability is applicable to structural health monitoring for monitoring mechanical deformation of structures such as large damage and crack propagation in structures.[43] Our hybrid photodetector with stretchability up to 200% can be developed for

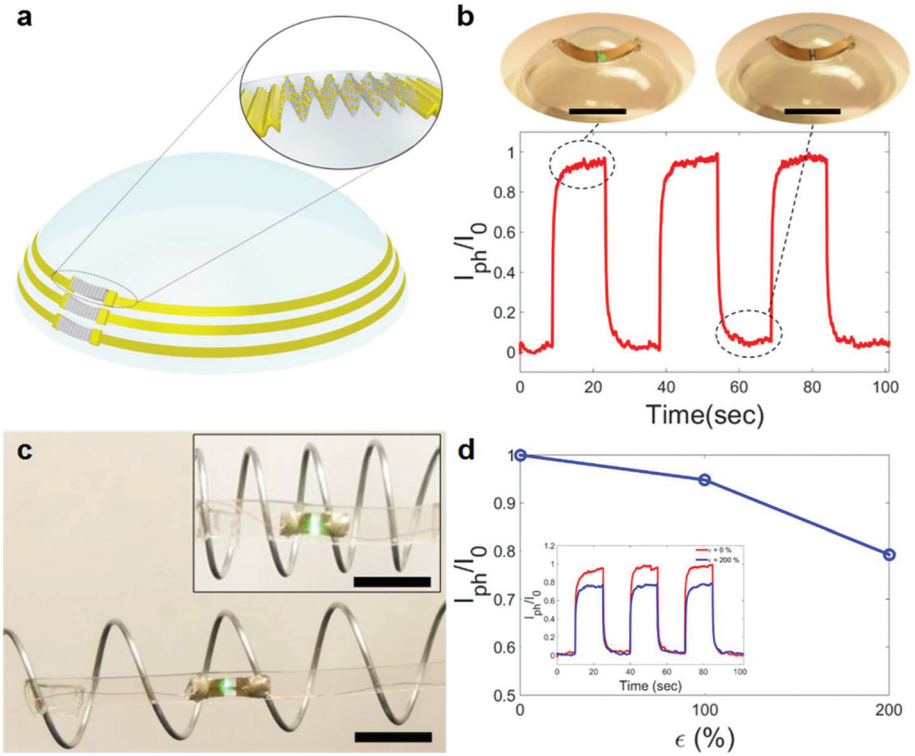

Fig. 4 Conformability and high stretchability of a hybrid photodetector with crumpled graphene–AuNP hybrid structures. (a) Schematic illustration of a stretchable hybrid photodetector integrated on a contact lens. (b) Dynamic photoresponse of the stretchable hybrid photodetector on a contact lens. Inset photographs show photoresponse measurements with the integrated hybrid photodetector at the illumination of a 532 nm laser light which is turned on (left) and off (right) (scale bar = 1 cm). (c) Photographs of a stretchable hybrid photodetector integrated on a spring for the demonstration of a dynamic mechanical strain sensing. Inset photograph shows the integrated photodetector at $\varepsilon_{tensile,x}$ = 0% (scale bars = 1 cm). (d) Measured photoresponse of the integrated hybrid photodetector at varying uniaxial tensile strains between 0% and 200%. Measured photocurrents were normalized by the photocurrent of the integrated hybrid photodetector measured at $\varepsilon_{tensile,x}$ = 0% (I_0). Inset figure shows dynamic photoresponse of the integrated hybrid photodetector at $\varepsilon_{tensile,x}$ = 0% and 200%.

detecting crack propagation with integration of a flexible light emitting diode and a wireless signal transmitting system.

Conclusions

In conclusion, we have demonstrated a novel approach to combining plasmonic enhancement with the crumpling of graphene for enhanced photoabsorption, and consequently, achieved the enhanced photoresponse of the crumpled hybrid photodetector. The highly enhanced and localized electrical fields induced around AuNPs and the areal density increase in graphene realized such an enhancement. Based on combined photoabsorption improvements, we have created the crumpled hybrid photodetector with ~12 times enhanced photoresponse *versus* the flat graphene photodetector. Moreover, the crumpled hybrid structure enabled outstanding mechanical stretchability up to 200%. We demonstrated the potential of our hybrid photodetector for applications such as an integrated optical sensor on a contact lens and a dynamic mechanical strain sensor. Integrating our high-performance stretchable photodetector has future potential for flexible integrated photonic devices and integrated wearable optical sensing devices.

Experimental methods

Material characterization

A scanning electron microscope (SEM) (S-4800, Hitachi, Japan) was used to qualitatively characterize the structure. A Raman spectrometer (Renishaw, UK) with a 633 nm laser was utilized to confirm the quality of the crumpled graphene at varying uniaxial strains between 0% and 200%. In Fig. 2d, the Raman spectral intensity of crumpled graphene without AuNPs was multiplied by five times. The Raman spectral intensity of the crumpled hybrid structures was much more intense due to the electromagnetic amplification of the Raman signal intensity by the plasmonic effect of the AuNPs.[39,49] The small peaks in the spectrum of crumpled graphene between ~2900 cm^{-1} and 3000 cm^{-1} were attributed to a VHB substrate. Ultraviolet-visible spectroscopy (Varian Cary 5G, US) was utilized to investigate the photoabsorption of the crumpled hybrid structure, crumpled graphene, and flat graphene. First, the transmittance values (T) of the crumpled hybrid structure, crumpled

graphene on VHB substrates under uniaxial tensile strains (0%–200%), and flat graphene on a VHB substrate were measured over a broad range of wavelengths (350 nm–800 nm). Then, the transmittance values (T_0) of bare VHB substrates over wavelengths (350 nm–800 nm) were obtained for background subtraction. The transmittance values were converted into extinction, which accounts for absorption and scattering, by calculating $1 - T/T_0$.

Device characterization

To characterize the photodetectors, the photocurrent of the device generated by the incident beam from a diode laser of 532 nm wavelength (power ~3 mW through a 5× objective lens) (CPS532, Thorlabs, NJ) was measured by using a source-meter (Keithley 2614B, OR) and microprobe station. To maintain a consistent power and illumination position, the laser power and beam focus/alignment were calibrated through a 5× objective lens with a photodiode power sensor (S120C and PM100USB, Thorlabs, NJ). The bias voltage of 15 μV was applied for the electrical potential through the gold electrodes, which is required to induce the current.

Acknowledgements

This work was supported by the Air Force Office of Scientific Research/Asian Office of Aerospace Research Development (AFOSR/AOARD) Nano Bio Info Technology (NBIT) Phase III Program (AOARD-13-4125), the AFOSR under award number FA9550-16-1-0251, the National Science Foundation (NSF) CAREER Award 1554019, and the Early Career Faculty grant (NNX16AR56G) from NASA's Space Technology Research Grants Program. Optical characterization techniques including SEM, Raman spectroscopy, and UV-Vis spectroscopy, as well as partial device fabrication, were carried out in the Frederick Seitz Materials Research Laboratory Central Research Facilities, and the Micro and NanoTechnology Laboratory at the University of Illinois at Urbana-Champaign.

References

1 C. L. Yu, H. Kim, N. de Leon, I. W. Frank, J. T. Robinson, M. McCutcheon, M. Liu, M. D. Lukin, M. Loncar and H. Park, *Nano Lett.*, 2013, **13**(1), 248–252.
2 D. H. Kim, N. Lu, R. Ma, Y.-S. Kim, R.-H. Kim, S. Wang, J. Wu, S. M. Won, H. Tao, A. Islam, K. J. Yu, T. Kim, R. Chowdhury, M. Ying, L. Xu, M. Li, H.-J. Chung, H. Keum, M. McCormick, P. Liu, Y.-W. Zhang, F. G. Omenetto, Y. Huang, T. Coleman and J. A. Rogers, *Science*, 2011, **333**(6044), 838–843.
3 Z. Ma, *Science*, 2011, **333**(6044), 830–831.
4 Z. Yu, X. Niu, Z. Liu and Q. Pei, *Adv. Mater.*, 2011, **23**(34), 3989–3994.
5 L. G. Ge, X. W. Wang, H. C. Chen, K. Q. Qiu and S. F. Fu, *Chin. Opt. Lett.*, 2012, **10**(9), 090502–090505.
6 K. C. Martinez-Anton, H. Canabal, J. A. Quiroga, E. Bernabeu, M. A. Labajo and V. C. Testillano, *Opt. Express*, 2001, **8**(12), 649–654.
7 C. M. Lochner, Y. Khan, A. Pierre and A. C. Arias, *Nat. Commun.*, 2014, **5**, 5745.
8 A. K. Geim and K. S. Novoselov, *Nat. Mater.*, 2007, **6**(3), 183–191.
9 C. Lee, X. Wei, J. W. Kysar and J. Hone, *Science*, 2008, **321**(5887), 385–388.
10 N. Liu, H. Tian, G. Schwartz, J. B. Tok, T. L. Ren and Z. Bao, *Nano Lett.*, 2014, **14**(7), 3702–3708.
11 A. Pospischil, M. M. Furchi and T. Mueller, *Nat. Nanotechnol.*, 2014, **9**(4), 257–261.
12 C. H. Liu, Y. C. Chang, T. B. Norris and Z. Zhong, *Nat. Nanotechnol.*, 2014, **9**(4), 273–278.
13 A. Pospischil, M. Humer, M. M. Furchi, D. Bachmann, R. Guider, T. Fromherz and T. Mueller, *Nat. Photonics*, 2013, **7**(11), 892–896.
14 J. M. Dawlaty, S. Shivaraman, M. Chandrashekhar, F. Rana and M. G. Spencer, *Appl. Phys. Lett.*, 2008, **92**(4), 042116.
15 D. Brida, A. Tomadin, C. Manzoni, Y. J. Kim, A. Lombardo, S. Milana, R. R. Nair, K. S. Novoselov, A. C. Ferrari, G. Cerullo and M. Polini, *Nat. Commun.*, 2013, **4**, 1987.
16 K. S. Kim, Y. Zhao, H. Jang, S. Y. Lee, J. M. Kim, K. S. Kim, J.-H. Ahn, P. Kim, J.-Y. Choi and B. H. Hong, *Nature*, 2009, **457**(7230), 706–710.
17 A. B. Kuzmenko, E. van Heumen, F. Carbone and D. van der Marel, *Phys. Rev. Lett.*, 2008, **100**(11), 117401.
18 R. R. Nair, P. Blake, A. N. Grigorenko, K. S. Novoselov, T. J. Booth, T. Stauber, N. M. R. Peres and A. K. Geim, *Science*, 2008, **320**(5881), 1308–1308.
19 M. C. Wang, S. Chun, R. S. Han, A. Ashraf, P. Kang and S. Nam, *Nano Lett.*, 2015, **15**(3), 1829–1835.
20 K. Yong, A. Ashraf, P. Kang and S. Nam, *Sci. Rep.*, 2016, **6**, 24890.
21 P. Kang, M. C. Wang, P. M. Knapp and S. Nam, *Adv. Mater.*, 2016, **28**(23), 4639–4645.
22 J. Zang, S. Ryu, N. Pugno, Q. Wang, Q. Tu, M. J. Buehler and X. Zhao, *Nat. Mater.*, 2013, **12**(4), 321–325.
23 M. Furchi, A. Urich, A. Pospischil, G. Lilley, K. Unterrainer, H. Detz, P. Klang, A. M. Andrews, W. Schrenk, G. Strasser and T. Mueller, *Nano Lett.*, 2012, **12**(6), 2773–2777.
24 M. Engel, M. Steiner, A. Lombardo, A. C. Ferrari, H. V. Lohneysen, P. Avouris and R. Krupke, *Nat. Commun.*, 2012, **3**, 906.
25 R.-J. Shiue, X. Gan, Y. Gao, L. Li, X. Yao, A. Szep, D. Walker, J. Hone and D. Englund, *Appl. Phys. Lett.*, 2013, **103**(24), 241109.
26 X. Gan, R.-J. Shiue, Y. Gao, I. Meric, T. F. Heinz, K. Shepard, J. Hone, S. Assefa and D. Englund, *Nat. Photonics*, 2013, **7**(11), 883–887.
27 X. Wang, Z. Cheng, K. Xu, H. K. Tsang and J.-B. Xu, *Nat. Photonics*, 2013, **7**(11), 888–891.
28 M. Jablan, M. Soljacic and H. Buljan, *Proc. IEEE*, 2013, **101**(7), 1689–1704.

29 J. Mertens, A. L. Eiden, D. O. Sigle, F. Huang, A. Lombardo, Z. Sun, R. S. Sundaram, A. Colli, C. Tserkezis, J. Aizpurua, S. Milana, A. C. Ferrari and J. J. Baumberg, *Nano Lett.*, 2013, **13**(11), 5033–5038.
30 T. J. Echtermeyer, L. Britnell, P. K. Jasnos, A. Lombardo, R. V. Gorbachev, A. N. Grigorenko, A. K. Geim, A. C. Ferrari and K. S. Novoselov, *Nat. Commun.*, 2011, **2**, 458.
31 Y. Liu, R. Cheng, L. Liao, H. Zhou, J. Bai, G. Liu, L. Liu, Y. Huang and X. Duan, *Nat. Commun.*, 2011, **2**, 579.
32 C. W. Chiang, G. Haider, W. C. Tan, Y. R. Liou, Y. C. Lai, R. Ravindranath, H. T. Chang and Y. F. Chen, *ACS Appl. Mater. Interfaces*, 2016, **8**(1), 466–471.
33 G. Konstantatos, M. Badioli, L. Gaudreau, J. Osmond, M. Bernechea, F. P. Garcia de Arquer, F. Gatti and F. H. Koppens, *Nat. Nanotechnol.*, 2012, **7**(6), 363–368.
34 Z. Sun, Z. Liu, J. Li, G. A. Tai, S. P. Lau and F. Yan, *Adv. Mater.*, 2012, **24**(43), 5878–5883.
35 Y. Pei, R. Pei, X. Liang, Y. Wang, L. Liu, H. Chen and J. Liang, *Sci. Rep.*, 2016, **6**, 21551.
36 C. Yan, J. Wang, X. Wang, W. Kang, M. Cui, C. Y. Foo and P. S. Lee, *Adv. Mater.*, 2014, **26**(6), 943–950.
37 J. Yoo, S. Jeong, S. Kim and J. H. Je, *Adv. Mater.*, 2015, **27**(10), 1712–1717.
38 W. Zhang, C. P. Chuu, J. K. Huang, C. H. Chen, M. L. Tsai, Y. H. Chang, C. T. Liang, Y. Z. Chen, Y. L. Chueh, J. H. He, M. Y. Chou and L. J. Li, *Sci. Rep.*, 2014, **4**, 3826.
39 J. Leem, M. C. Wang, P. Kang and S. Nam, *Nano Lett.*, 2015, **15**(11), 7684–7690.
40 M. Kang, S.-G. Park and K.-H. Jeong, *Sci. Rep.*, 2015, **5**, 14790.
41 M. E. Fitzgerald, B. A. Vana and A. Reiner, *Invest. Ophthalmol. Visual Sci.*, 1990, **31**(12), 2483–2492.
42 G. T. Feke, A. Yoshida and C. L. Schepens, *J. Biomed. Opt.*, 1998, **3**(4), 415–422.
43 D. Ryu, K. J. Loh, R. Ireland, M. Karimzada, F. Yaghmaie and A. M. Gusman, *Smart Struc. Syst.*, 2011, **8**(5), 471–486.
44 P. Xu, J. Kang, J. Suhr, J. P. Smith, K. S. Booksh, B. Wei, J. Yu, F. Li, J.-H. Byun, Y. Oh and T.-W. Chou, *Carbon*, 2015, **93**, 620–624.
45 J. Song, H. Jiang, W. M. Choi, D. Y. Khang, Y. Huang and J. A. Rogers, *J. Appl. Phys.*, 2008, **103**(1), 014303.
46 T. Tamura, Y. Maeda, M. Sekine and M. Yoshida, *Electronics*, 2014, **3**(2), 282–302.
47 A. V. Thomas, B. C. Andow, S. Suresh, O. Eksik, J. Yin, A. H. Dyson and N. Koratkar, *Adv. Mater.*, 2015, **27**(21), 3256–3265.
48 A. Hohenau, J. R. Krenn, J. Beermann, S. I. Bozhevolnyi, S. G. Rodrigo, L. Martin-Moreno and F. Garcia-Vidal, *Phys. Rev. B: Condens. Matter*, 2006, **73**(15), 155404.
49 W. Xu, X. Ling, J. Xiao, M. S. Dresselhaus, J. Kong, H. Xu, Z. Liu and J. Zhang, *Proc. Natl. Acad. Sci. U. S. A.*, 2012, **109**(24), 9281–9286.